



Predicting indenter nose shape sensitivity for quasi-static perforation of thin metallic plates



I. Mohagheghian^{*}, W.J. Stronge, G.J. McShane

Department of Engineering, University of Cambridge, Trumpington Street, Cambridge CB2 1PZ, UK

ARTICLE INFO

Article history:

Received 6 June 2016

Received in revised form

30 August 2016

Accepted 2 September 2016

Available online 3 September 2016

Keywords:

Thin metals

Perforation

Nose shape dependency

Lode parameter

ABSTRACT

Perforation resistance is an important design consideration for thin-walled metallic structures. However, the perforation energy of thin metallic plates is known to be sensitive to the nose shape of the indenter. This poses a challenge for predictive modelling, both analytical and numerical, as the material deformation and state of stress at the onset of failure can vary significantly from one indenter geometry to the next. Effective design requires an understanding of the key modelling parameters, and their influence on the predicted perforation response, across the widest range of possible indenter geometries. This paper aims to investigate systematically the indenter nose shape sensitivity of the quasi-static perforation of a 1 mm thick plate of aluminium alloy 6082-T4, and the modelling of the conditions at failure. The nose shape of the indenter is gradually changed from flat (i.e. blunt) to hemi-spherical either by (i) introducing a chamfer at the edge of the indenter or (ii) by changing the indenter frontal nose radius. This allows a wide range of states of deformation at the onset of failure to be spanned. The problem is investigated by both analytical and numerical methods. The results of both modelling techniques are compared with quasi-static perforation experiments, and the conditions necessary to achieve good agreement are obtained. Careful consideration of (i) material anisotropy, (ii) indenter-plate friction and (iii) boundary compliance is necessary for accurate prediction of the perforation energy. A Lode angle-dependent model for the onset of failure in the metal is found to be essential for predicting the perforation response for a range of indenter chamfer radii.

© 2016 The Authors. Published by Elsevier Masson SAS. This is an open access article under the CC BY license (<http://creativecommons.org/licenses/by/4.0/>).

1. Introduction

The perforation resistance of thin-walled metallic structures, for both quasi-static and impact loading, is known to strongly depend on the nose shape of the indenter. The tip geometry controls the mode of deformation, and the type and distribution of fracture observed during the perforation. Four types of indenter nose shape have formed the focus of most previous investigations of perforation: flat (i.e. blunt), hemi-spherical, conical and ogival tips. These induce contrasting failure mechanisms in the target. For most studies of thin, ductile metallic plates reported in the literature, perforation resistance is highest for a hemi-spherical nose shape (Corran et al., 1983; Gupta et al., 2007; Kpenyigba et al., 2013). In this case, failure is by tensile tearing, which is observed to dissipate more energy than alternative failure mechanisms such as shear plugging or discing (Grytten et al., 2009; Langseth and Larsen, 1994;

Liu and Stronge, 2000) for flat-nosed, or petal bending for conical- and ogival-tipped indenters (Iqbal et al., 2010; Landkof and Goldsmith, 1985; Leppin and Woodward, 1986).

The transition between different failure modes and its effect on the perforation resistance have been investigated in the literature by gradually changing the nose shape from one to another (e.g. flat to hemi-spherical). Corran et al. (1983) conducted a series of impact tests on 1.3 mm mild steel targets – their tests used a 12.5 mm diameter projectile. They progressively changed the ratio of the projectile radius to the tip radius (R_i/R_f) from 0 to 1, corresponding to the limits of a blunt and a hemi-spherical tip, respectively (Fig. 1a). It was observed that failure occurs by plugging when $R_i/R_f < 0.52$. On the other hand, for larger ratios (e.g. $R_i/R_f = 0.66–1$) failure occurs by tensile tearing. Their results show a maximum in the perforation energy at a tip geometry for which the transition between these two failure modes occurs.

A similar change in the failure mode was also observed by Teng and Wierzbicki (2005) by altering the size of the chamfer (R_{ch}) on a circular cylindrical projectile of radius R_i (Fig. 1b). Their numerical

^{*} Corresponding author.

E-mail address: i.mohagheghian@cantab.net (I. Mohagheghian).

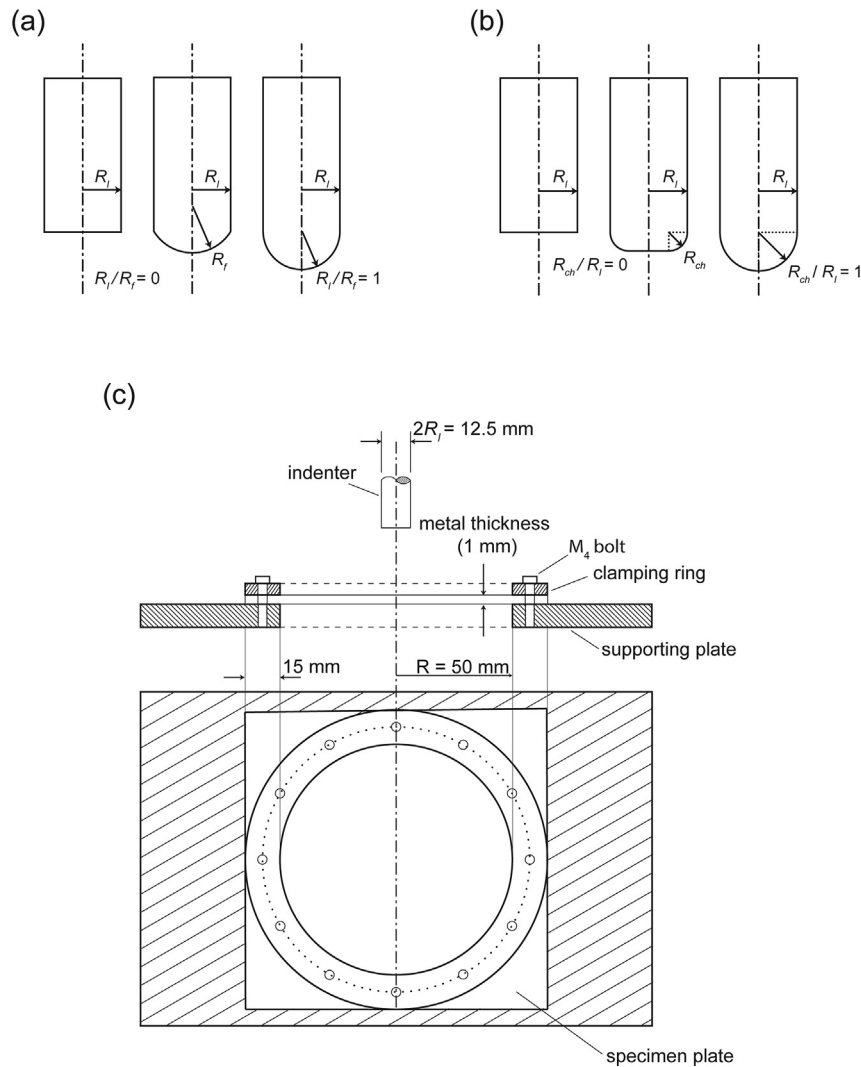


Fig. 1. Schematic of the two indenter nose shape types, permitting a transition from a flat to a hemi-spherical indenter by (a) changing the frontal nose radius (R_f) and (b) introducing different chamfer radii (R_{ch}). (c) The plate clamping arrangements for the punch indentation tests.

results suggest that while shear plugging occurs under a blunt projectile (i.e. $R_{ch}/R_l = 0$), the failure mode changes to tensile failure for $R_{ch}/R_l = 0.5$. Note that a hemi-spherical tip corresponds to $R_{ch}/R_l = 1$. Iqbal et al. (2010) numerically investigated the effect of changing the nose shape on the ballistic limit and failure modes of metallic targets. They changed the projectile nose shape from flat to hemi-spherical and ogival by changing R_{ch} in the range $0 \leq R_{ch}/R_l \leq 5$. Values of $R_{ch}/R_l > 1$ represent ogive nosed projectiles (Iqbal et al., 2010). Their results for 1 mm thickness aluminium targets suggest that the ballistic limit increases as the tip is changed from a blunt to a hemi-spherically tip projectile, and then significantly drops for ogive nosed projectiles. For $R_{ch}/R_l > 2$, the ballistic limit becomes less sensitive to further increases in the chamfer radius.

In all of the above studies, the failure mode transition was achieved by changing the shape of a non-deformable indenter (or projectile). However, for a single nose shape, a change in the failure mode can also be observed if a more deformable indenter is used. Liu and Stronge (2000) investigated the effect of projectile deformability on the failure modes and ballistic limit of metallic targets. The projectiles were all initially blunt and had the same mass, but were made from different materials, including pure aluminium, two types of aluminium alloy and PTFE. By decreasing

the material strength, more deformation (normally called ‘mushrooming’) occurred in the projectile. As a result, both the diameter and tip radius of the projectile change. This has a direct effect on the failure mode in the metal target. For a projectile with higher strength, shear failure is most likely to occur. Conversely, for more deformable projectiles, tensile tearing is more favourable. The increase in the ballistic limit for softer projectiles is considered to be the result of more dishing in the plate (Liu and Stronge, 2000). The mushroomed nose observed for softer projectiles caused larger curvatures at the periphery of the contact region which reduced the shear strains (Liu and Stronge, 2000).

For a non-deformable indenter (or projectile), the effective nose shape can also be changed indirectly by placing a layer of a soft and deformable material in front of the target (e.g. in the case of polymer-metal bi-layers (Mohagheghian et al., 2016)). Deformation of this soft layer between the projectile and the metal backing changes the effective nose shape of the projectile, alters the failure mode and in turn increases the energy absorbed by the metal layer (Mohagheghian et al., 2016). This phenomenon is found to be very sensitive to the thickness of the soft layer and the initial indenter geometry (Mohagheghian et al., 2016). The biggest increase in the perforation energy is observed for a blunt indenter when the

thickness of the soft polymer layer is chosen carefully so that the failure mode of the metal layer is just at the transition from plugging to tensile failure, similar to the observation of Corran et al. (1983).

It can clearly be seen from the literature that the nose shape (or effective nose shape) of the indenter has a significant influence on the energy absorption capacity of a thin metallic plate. The shape of the indenter controls the strain distribution and stress state in the target. Therefore having a model capable of predicating the perforation energy for a wide range of nose shapes is essential especially when the effective nose shape is not known in advance (e.g. indentation in polymer-metal bi-layers).

The aim of this study is to investigate the indenter nose shape sensitivity for the quasi-static perforation of a 1 mm thick plate of aluminium alloy 6082-T4. The nose shape of the non-deforming indenter is gradually changed from flat to hemi-spherical in two distinct ways: (i) varying the tip radius (Fig. 1a) and (ii) introducing a variable chamfer radius to the edge of a blunt indenter (Fig. 1b). This produces a wide range of deformations and stress states at the onset of failure of the plate, between two well-understood end states: the blunt and the hemispherical-tip. Next, we aim to establish the critical modelling parameters required to predict the onset of failure accurately for the widest range of tip geometries. Both theoretical and numerical modelling strategies will be considered. The work provides a new contribution to the existing literature in this field, by identifying the criteria necessary for both of these modelling strategies to accurately predict the response over a wide range of indenter nose shapes. This is especially important (i) when the same model is to be applied to a range of loading scenarios without altering model parameters, and (ii) when the loading conditions are not known in advance, for example if the effective nose-shape of the indenter is altered by some other process (e.g. by a deformable coating facing the target).

The outline of this paper is as follows: In Section 2, the material characterisation and perforation experiments on a 1 mm thick aluminium alloy 6082-T4 plate are described. A theoretical analysis is proposed in Section 3 that considers the effect of changing the indenter nose shape. In Section 4, finite element analysis is employed to investigate further the effect of nose shape on the perforation resistance, providing further insights into the importance of material constitutive modelling parameters, boundary conditions and contact conditions. Finally, conclusions are drawn in Section 5.

2. Experimental

2.1. Material characterisation

Tensile tests were carried out on dog-bone specimens of the aluminium alloy 6082-T4 sheet. Specimens were machined with orientations parallel, perpendicular and at 45° to the rolling direction to assess the anisotropy of the material using the experimental technique reported by Beese et al. (2010). The geometry of the dog-bone specimens follows ASTM standard E8/E8m (ASTM E8/E8m-11, 2011): the length of the gauge section is 32 mm, the width is 6 mm and the sheet thickness is 1 mm. The tensile tests were conducted using an Instron screw driven test machine at a cross-head speed of 0.9 mm min⁻¹ (corresponding to a nominal strain rate of approximately 5 × 10⁻⁴ s⁻¹). A dark speckle pattern was sprayed onto a white background in the gauge area of the dog-bone specimens for the purpose of digital image correlation (DIC). A digital camera mounted close to the specimen recorded images with a resolution of 2048 × 1448 pixels every 0.25 s. This gives a resolution of 36 pixel/mm in the gauge area of the specimen.

To measure the in-plane strains, parallel and perpendicular to

the loading direction, deformation of a square of material inside the gauge section was monitored through consecutive images. The strains were obtained by post processing the images using a Matlab script reproduced from Eberl et al. (2006). To check the accuracy of the technique, the strains obtained with Digital Image Correlation (DIC) parallel to the loading direction were compared with the global strain measured using a laser extensometer while the deformation was homogenous inside the gauge section. A good match was observed. The tensile results in the three orientations are shown in Fig. 2. It can be seen that the in-plane anisotropy of the material is small.

In order to calculate the out-of-plane anisotropy, the Lankford's r-value approach (Beese et al., 2010; Lankford et al., 1950) is adopted here. The r-value corresponding to a specific in-plane angle is defined as the ratio of the transverse strain to the through thickness strain. Two orthogonal components of in-plane strain (parallel and perpendicular to the loading direction) were measured experimentally using the 2D DIC approach. The through thickness strain was calculated based on an assumption of conservation of volume. The r-value was found to be approximately independent of the applied strain throughout the phase of homogenous deformation before the onset of necking. The r-values obtained in three orientations with respect to the rolling direction are listed in Table 1.

Lankford's r-values are used to calculate the material constants for the Hill (1948) anisotropic yield criterion (Abaqus, 2010). The yield criterion can be expressed in terms of the components of the stress tensor σ_{ij} as follows:

$$\bar{\sigma}^2 = F(\sigma_{22} - \sigma_{33})^2 + G(\sigma_{33} - \sigma_{11})^2 + H(\sigma_{11} - \sigma_{22})^2 + 2L\sigma_{23}^2 + 2M\sigma_{31}^2 + 2N\sigma_{12}^2 = \sigma_0^2 \quad (1)$$

where F, G, H, L, M and N are material constants, $\bar{\sigma}$ is the equivalent stress and σ_0 is an arbitrary reference yield stress. In the case of plane stress condition ($\sigma_{23} = \sigma_{31} = \sigma_{12} = 0$), only F, G, H and N need to be determined based on the following equations:

$$F = \frac{1}{2} \left(\frac{1}{R_{22}^2} + \frac{1}{R_{33}^2} - \frac{1}{R_{11}^2} \right), \quad G = \frac{1}{2} \left(\frac{1}{R_{33}^2} + \frac{1}{R_{11}^2} - \frac{1}{R_{22}^2} \right), \quad H = \frac{1}{2} \left(\frac{1}{R_{11}^2} + \frac{1}{R_{22}^2} - \frac{1}{R_{33}^2} \right) \quad \text{and} \quad N = \frac{3}{2R_{12}^2} \quad (2)$$

R_{11}, R_{22}, R_{33} and R_{12} are anisotropic yield stress ratios defined as:

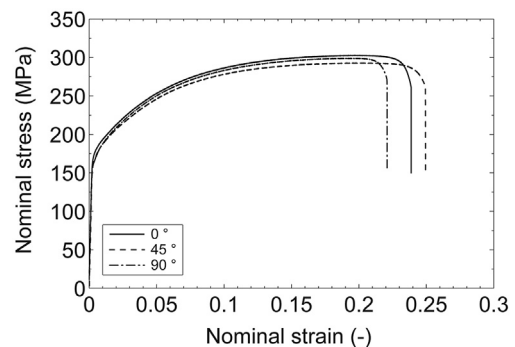


Fig. 2. The quasi-static uniaxial tensile response of 1 mm thick aluminium alloy 6082-T4 sheet in three different orientations relative to the rolling direction.

Table 1

Material model parameters measured for aluminium alloy 6082-T4.

Lankford's r values			Anisotropy constants for Hill (1948) anisotropic yield						Coefficients of power law isotropic hardening	
$r_0(-)$	$r_{45}(-)$	$r_{90}(-)$	$R_{11}(-)$	$R_{22}(-)$	$R_{33}(-)$	$R_{12}(-)$	$R_{13}(-)$	$R_{23}(-)$	A (MPa)	$n(-)$
0.52	0.62	0.53	1	1.01	0.876	1.01	1	1	480	0.19

$$R_{11} = \frac{Y_{11}}{\sigma_0}, R_{22} = \frac{Y_{22}}{\sigma_0}, R_{33} = \frac{Y_{33}}{\sigma_0}, R_{12} = \sqrt{3} \frac{Y_{12}}{\sigma_0} \quad (3)$$

where Y_{ij} is the measured yield stress value and σ_0 is the arbitrary reference yield stress. By considering $\sigma_0 = Y_{11}$, the anisotropic yield stress ratios are given by:

$$R_{11} = 1, R_{22} = \sqrt{\frac{r_{90}(r_0 + 1)}{r_0(r_{90} + 1)}}, R_{33} = \sqrt{\frac{r_{90}(r_0 + 1)}{(r_0 + r_{90})}}, R_{12} = \sqrt{\frac{3r_{90}(r_0 + 1)}{(2r_{45} + 1)(r_0 + r_{90})}}, \quad (4)$$

and their values are listed in Table 1.

2.2. Perforation experiments

Quasi-static perforation experiments were conducted using an Instron screw driving test machine. Indenters with diameter 12.5 mm and different nose shapes, as illustrated in Fig. 1, were mounted to the load cell on the cross-head of the machine. The test specimen plates were circular, of diameter 100 mm, with clamped boundary conditions. To achieve this, square, flat, aluminium alloy specimen plates with dimensions 130 × 130 mm were clamped using a circular steel ring with an internal diameter of 100 mm and thickness of 5 mm (Fig. 1c). Twelve M4 bolts were used to fasten this clamping ring to a supporting steel plate (thickness 10 mm) through clearance holes (Fig. 1c). The indentation tests were performed at a cross head speed of 1 mm min⁻¹, and were stopped on the initiation of fracture in the specimen plate. The indentation force was recorded by the load cell, and the indenter displacement was obtained from the cross head displacement.

Two configurations of indenter are considered in this investigation: one having a variable frontal nose radius (R_f), shown in Fig. 1a, and one having a variable chamfer radius (R_{ch}), as illustrated in Fig. 1b. For indenters with variable chamfer radii, five different radii were considered: $R_{ch} = 0, 1.5, 3, 4.5$ and 6.25 mm. The chamfer radii $R_{ch} = 0$ and 6.25 mm correspond to a blunt (i.e. flat) and a hemi-spherical indenter respectively. The force-displacement curves measured during indentation are shown in Fig. 3a. Increasing the chamfer radius causes a reduction in the slope of the curves. On the other hand, the plate failure is postponed to a larger indenter displacement which results in a monotonic increase in the total energy absorption up to fracture (E_A), defined as the area under the indenter force-displacement curve (Fig. 3c).

For indenters with variable frontal nose radii, four different values were tested: $R_f = 7.5, 9, 12$ and 30 mm. The cases $R_f = \infty$ and 6.25 mm correspond to the blunt and hemi-spherical cases, as described above. The indenter force-displacement curves are shown in Fig. 3b. Similar to Fig. 3a, the slope of the curves gradually reduces as the tip is changed from flat to hemi-spherical. However, the peak force and displacement at failure both reach a maximum at $R_f = 9$ mm. This results in a maximum in the total energy absorption up to fracture at that radius, as shown in Fig. 3d. Inspection

of failed plates indicates a transition in the failure mode, from plugging to tensile failure, at this radius as suggested by Corran et al. (1983).

3. Theoretical analysis

The aim of this section is to investigate whether the experimental observations in Section 2.2 (including the indenter force-displacement history, the displacement at failure and the total energy absorption) can be captured by a computationally efficient theoretical model. In this section, an axis-symmetric theoretical model is proposed, based on that of Simonsen and Lauridsen (2000) for a hemi-spherical indenter, but extended in order to account for the variations in the indenter nose shape considered here. The effect of introducing material anisotropy in the model also will be discussed.

A schematic of the two types of the indenter (discussed in Section 2.2) is shown in Fig. 4, defining the geometry parameters to be used in the model. The problem is considered to be axis-symmetric, employing the (r, θ, z) coordinate shown in Fig. 4. R_i and t are the indenter radius and the plate thickness, respectively. The indenter is assumed to be in contact with the plate over the region $0 < r < r_c$, where the radial coordinate r is measured to the mid-plane of the plate. ψ_c is the wrapping angle that corresponds to the plate rotation at point $r = r_c$ and $\psi(r)$ is the angle of rotation of the plate at any point outside of the contact area, $r > r_c$. The plate is circular, with radius R , and is clamped at its boundary (not shown in Fig. 4), such that the displacement and rotation of the plate are zero at $r = R$.

The plate is considered to be in a state of plane stress, and variations in stress through the plate thickness due to bending are neglected (valid for thin plates, deforming in a 'membrane' mode). It is also assumed that the in-plane components of displacement for the plate are zero, with each point moving only in a transverse direction (i.e. along the z axis in Fig. 4) (Lee et al., 2004; Simonsen and Lauridsen, 2000). Furthermore, incompressible deformation of the plate material is assumed throughout. As a result of these assumptions, the stress and strain components are given by:

$$\sigma_{zz} = \sigma_{rz} = \sigma_{\theta z} = 0 \quad (5)$$

$$\varepsilon_{\theta\theta} = \varepsilon_{r\theta} = \varepsilon_{\theta z} = 0, \quad \varepsilon_{rr} = -\varepsilon_{zz} = \ln\left(\frac{1}{\cos \psi}\right). \quad (6)$$

The material is taken to obey power law hardening, as follows:

$$\bar{\sigma} = C_0 \bar{\varepsilon}^n \quad (7)$$

where C_0 and n are material constants and $\bar{\sigma}$ and $\bar{\varepsilon}$ are the equivalent stress and strain, respectively. The equivalent strain for general 3D loading can be expressed as (Colby, 2013):

$$d\bar{\varepsilon} = \sqrt{\frac{F d\varepsilon_{rr}^2 + G d\varepsilon_{\theta\theta}^2 + H d\varepsilon_{zz}^2}{FG + FH + GH} + \frac{2 d\varepsilon_{\theta z}^2}{L} + \frac{2 d\varepsilon_{zr}^2}{M} + \frac{2 d\varepsilon_{r\theta}^2}{N}}. \quad (8)$$

Assuming principal stresses to be aligned with r, θ and z

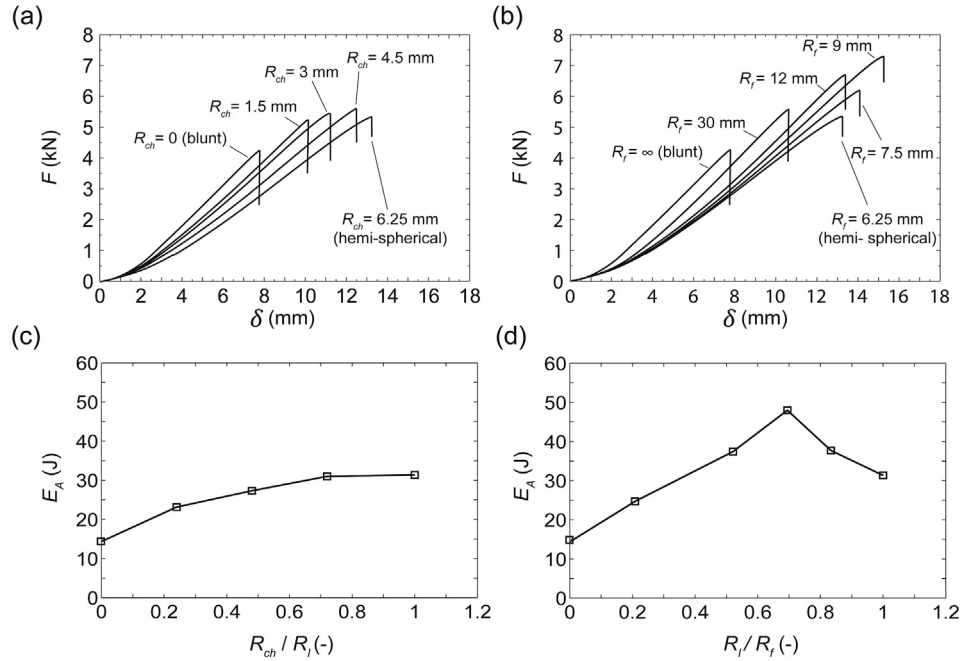


Fig. 3. Quasi-static indentation response of aluminium alloy 6082-T4 plates (thickness $h_m = 1$ mm) loaded by indenters with different (a) R_{ch} and (b) R_f . δ is the indenter displacement and F is the indenter force. (c) and (d) show the energy absorption up to fracture (E_A) for indenters with different R_{ch} and R_f , respectively.

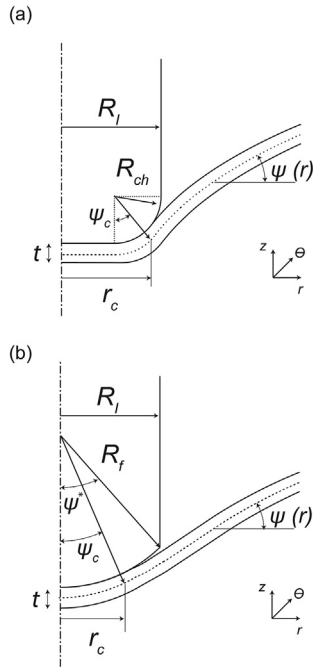


Fig. 4. Geometrical representation of parameters used for the theoretical model for two types of indenter (a) with a chamfer at the edge and (b) with a frontal nose radius.

directions and considering Equation (5), the equivalent stress $\bar{\sigma}$ in Equation (1) can be expressed as:

$$F\sigma_{\theta\theta}^2 + G\sigma_{rr}^2 + H(\sigma_{rr} - \sigma_{\theta\theta})^2 = \bar{\sigma}^2. \quad (9)$$

Since $R_{11} = R_{22} \cong 1$ then

$$F = G = 1 - H = \frac{1}{2} \left(\frac{1}{R_{33}^2} \right), \quad (10)$$

and the expression for equivalent stress is simplified to:

$$\sigma_{\theta\theta}^2 + \sigma_{rr}^2 - 2(1 - F)\sigma_{rr}\sigma_{\theta\theta} = \bar{\sigma}^2. \quad (11)$$

The associated flow rule, in combination with the assumption that $\varepsilon_{\theta\theta} = 0$, results in:

$$\sigma_{\theta\theta} = H \sigma_{rr} \quad (12)$$

and consequently:

$$\bar{\sigma} = \sqrt{F(2 - F)} \sigma_{rr}. \quad (13)$$

Using Equations (6) and (10), Equation (8) also simplifies to:

$$d\bar{\varepsilon} = \sqrt{\frac{1}{F(2 - F)}} d\varepsilon_{rr}. \quad (14)$$

Based on Equations (7), (13) and (14), the relationship between the radial components of stress and strain, considering anisotropy, can be expressed as:

$$\sigma_{rr} = KC_0 \varepsilon_{rr}^n \quad (15)$$

where

$$K = \frac{1}{\sqrt{F(2 - F)}} \left(\sqrt{\frac{1}{F(2 - F)}} \right)^n. \quad (16)$$

Equilibrium in the vertical direction (the z -direction in Fig. 4) requires that the indenter force:

$$P = 2\pi r \sigma_{rr} t \sin \psi. \quad (17)$$

From Equation (6), the plate thickness $t = t_0 \cos \psi$, where t_0 is the undeformed thickness. Combining these results leads to:

$$P = 2\pi K C_0 t_0 r [-\ln \cos \psi]^n \cos \psi \sin \psi \quad (18)$$

3.1. Variable chamfer radii

Considering first the geometry of indenter shown in Fig. 4a, the radius r_c (measured to the mid-plane of the plate) can be expressed as follows:

$$r_c = (R_f - R_{ch}) + \left(R_{ch} + \frac{t_0 \cos \psi_c}{2} \right) \sin \psi_c. \quad (19)$$

Using (18), and considering equilibrium over the contact patch, the indenter force can be written:

$$P = 2\pi K C_0 t_0 r_c [-\ln \cos \psi_c]^n \cos \psi_c \sin \psi_c. \quad (20)$$

The indenter displacement δ is given by:

$$\delta(\psi_c) = \left(R_{ch} + \frac{t_0 \cos \psi_c}{2} \right) (1 - \cos \psi_c) + \int_{r_c}^R \tan \psi(r, \psi_c) dr. \quad (21)$$

The plate angle variation outside of the contact patch, $\psi(r, \psi_c)$ in Equation (21), can be obtained for any ψ_c by substituting for the indenter force from Equation (20) into Equation (18). The resulting non-linear equation is then solved numerically. The displacement at the point of failure can be obtained by considering the global stability criterion suggested by Simonsen and Lauridsen (2000): $\partial P / \partial \psi_c = 0$. The wrapping angle at the point of failure ψ_{cf} is therefore obtained by differentiating Equation (20) and solving the resulting non-linear equation numerically. Hence, ψ_{cf} and consequently $\delta(\psi_{cf})$ is a function of the indenter radius (R_f), chamfer radius (R_{ch}), the hardening constant n and the initial thickness of the plate t_0 .

Next, the model predictions are compared against the experimental results. A power law curve (Equation (7)) was fitted through the true stress-true strain data for aluminium alloy 6082-T4, giving $C_0 = 480$ MPa and $n = 0.19$. The indenter force versus displacement, and the indenter displacement at the onset of failure, were calculated using the above relationships. The results are plotted for comparison with the experimental data in Fig. 5 for a single tip geometry: the hemi-spherical case ($R_{ch} = 6.25$ mm). For aluminium alloy 6082-T4, if the anisotropy of the material is taken into account, $R_{33} = 0.876$ and, according to Equation (16), $K = 1.08$. If the material is assumed isotropic, (i. e. $R_{33} = 1$) the Hill yield criterion, Equation (1), reduces to the von Mises criterion. As a result, $\sigma_{\theta\theta} = 0.5 \sigma_{rr}$ (Equation (12)) and $K = 1.19$ (Equation (16)). Note that the value of K , and hence the material anisotropy, influences the indenter force calculation, Equation (20), but does not affect the expressions for the indenter displacement, Equation (21), or the displacement at failure. As can be seen in Fig. 5, anisotropy reduces the slope of the curve.

Recall that the current model assumes that the tangential strain under the indenter $\varepsilon_{\theta\theta} = 0$. An alternative approach is to assume that $\sigma_{\theta\theta}$ has no influence on yielding of the material under the indenter (the limited interaction curve concept used by (Lee et al., 2004; Simonsen and Lauridsen, 2000)). In this case, the constant $K = 1$. This reduces the slope of the curve further. However, according to Equations (11–12), under plain strain condition $\sigma_{\theta\theta}$ makes a considerable contribution to the value of the effective stress, and consequently yielding of the material. As a result, for consistency with our kinematic assumptions ($\varepsilon_{\theta\theta} = 0$), the value

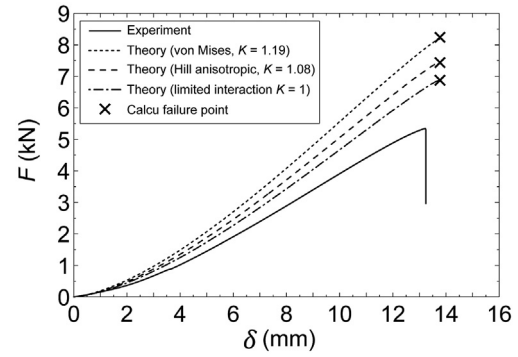


Fig. 5. The effect of the choice of yield surface on the theoretical model predictions of the indentation response (indenter force F against indenter displacement δ) of a 1 mm thick aluminium alloy 6082-T4 plate perforated by a hemi-spherical indenter. The model predictions are compared with experimental results.

$K = 1.08$ will be considered in subsequent comparisons with experiment.

Model predictions, including material anisotropy, for five different chamfer radii ($R_{ch} = 0, 1.5, 3.0, 4.5$ and 6.25 mm) are compared with experimental results in Fig. 6a. The model successfully predicts the change in the slope of the curve with variations in the chamfer radius. However, for all nose shapes, the theory predicts a larger gradient. The indenter displacement at the onset of failure δ_f is plotted in Fig. 6b. Good agreement can be observed when R_{ch} value is close to the radius of the indenter. Although the theoretical model captures a reduction in δ_f with decreasing R_{ch} , the calculated values are still higher than experimental results. The discrepancy becomes larger as R_{ch} approaches zero. This has a direct consequence on the perforation energy in Fig. 6c, as defined by the area under force-displacement curve. It should be noted however, that the choice of K has a relatively small influence on the total energy absorption predicted by the model (Fig. 6c).

3.2. Variable frontal nose radii

Now consider the second family of indenter tip geometries, sketched in Fig. 4b, where the frontal nose radius of the indenter is varied from $R_f = \infty$ (i.e. a flat, or blunt, face) to $R_f = R_l$ (a hemi-spherical tip). A similar analysis approach is applied to this tip geometry. Let the angle ψ_c , measured relative to the indenter centre-line, define the segment of the tip in contact with the plate, and angle ψ^* define the edge of the tip, as shown in Fig. 4b. The latter is given by:

$$\psi^* = \arcsin \left(\frac{R_l}{R_f} \right). \quad (22)$$

The radius of contact, again measured to the plate centre-line, is given by:

$$r_c = \left(R_f + \frac{t}{2} \right) \sin \psi_c. \quad (23)$$

Adopting the same kinematical assumptions and material hardening law for the plate deformation as outlined in Section 3.1, the indenter force and displacement are given by:

$$P = 2\pi K C_0 t_0 \left(R_f + \frac{t_0 \cos \psi_c}{2} \right) [-\ln \cos \psi_c]^n \cos \psi_c \sin^2 \psi_c. \quad (24)$$

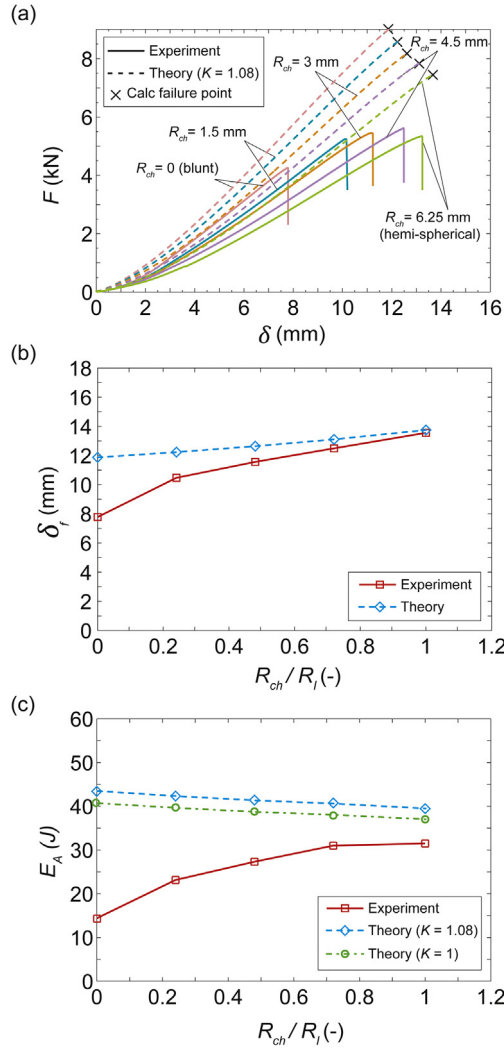


Fig. 6. Comparison between experimental results and theoretical model predictions, assuming anisotropic plasticity ($K = 1.08$), for (a) indenter force F against indenter displacement δ , (b) displacement at failure δ_f and (c) absorbed energy E_A for $0 \leq R_{ch}/R_f \leq 1$. (c) also shows the effect of the modelling constant K on the predicted energy absorption.

$$\delta = \left(R_f + \frac{t_0 \cos \psi_c}{2} \right) (1 - \cos \psi_c) + \int_{r_c}^R \tan \psi dr. \quad (25)$$

The method for calculating the plate rotation ψ for $r_c < r \leq R$ is outlined in Section 3.1. The onset of failure in the plate is again assumed to be given by the stability criterion $\partial P / \partial \psi_c = 0$ (Simonsen and Lauridsen, 2000), with the arc length of the contact patch at failure defined by the angle ψ_{cf} . Evaluating this derivative indicates that when t_0 is small, ψ_{cf} becomes independent of R_f and tends to the result for a hemi-spherical tip.

The above model is valid as long as $\psi_c \leq \psi^*$ at the onset of failure. A further refinement is necessary if the point of contact reaches the edge of the indenter tip (at ψ^*) before the failure criterion is met. For the material model used here (aluminium alloy 6082-T4) this occurs for $R_f/R_f < 0.86$. In this case the plate is assumed to subsequently wrap around the edge of the indenter with a radius equal to half the plate thickness (similar to the case in Section 3.1 when the chamfer radius is zero). The radius of the contact area thus remains constant at:

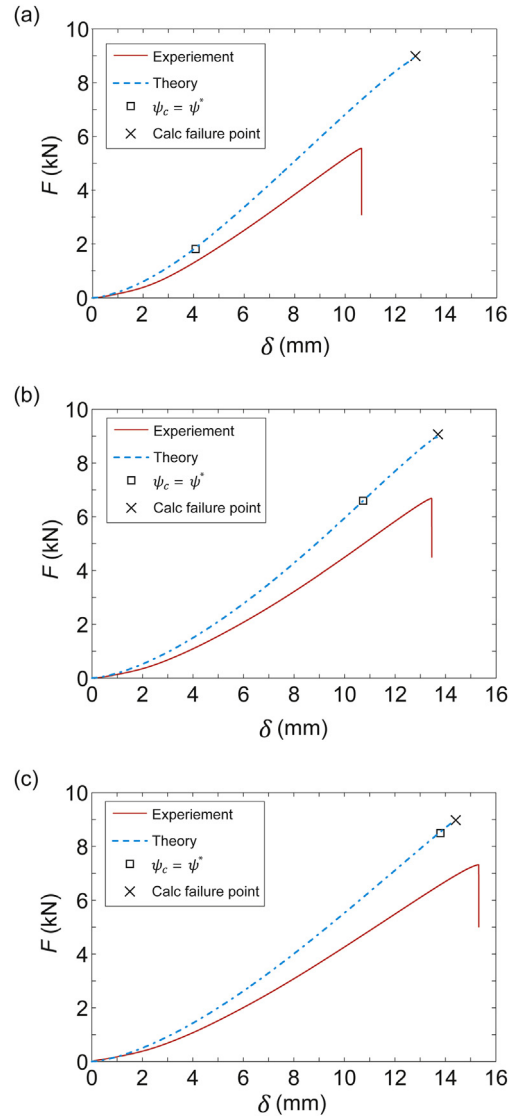


Fig. 7. Comparison between the experimental results and the theoretical model predictions of the indenter force F against indenter displacement δ for indenters with frontal nose radii of (a) $R_f = 30$, (b) $R_f = 12$ and (c) $R_f = 9$ mm ψ_c is the wrapping angle at the point of contact and ψ^* defines the edge of the tip.

$$r_c = R_f + \frac{t \sin \psi^*}{2}. \quad (26)$$

The indenter force is given by Equation (20). The indenter displacement in this phase can be calculated using Equation (25), with the substitution $\psi_c = \psi^*$.¹

The model predictions are compared with experimental results in Fig. 7 for three different frontal nose radii: $R_f = 30$, 12 and 9 mm. In all three cases the model over predicts the slope of the indenter force-deflection curve. For $R_f = 30$ mm (Fig. 7a), the plate comes into contact with the edge of the indenter ($\psi_c = \psi^*$) early in the deformation, at $\delta = 4$ mm, with failure predicted at $\delta_f = 12.7$ mm. In contrast, for $R_f = 9$ mm (Fig. 7c), $\psi_c = \psi^*$ occurs at a larger indenter

¹ Note that there is a narrow range of R_f/R_f ($0.79 < R_f/R_f < 0.86$) for the current material, Al alloy 6082-T4) for which the plate comes into contact with the edge of the indenter, but where ψ^* is greater than ψ_{cf} as calculated for the indenter with $R_{ch} = 0$. In this case ψ_{cf} is considered to be equal to ψ^* .

displacement (around 14 mm), close to the predicted onset of failure. Consistent with the results of Section 3.1, the discrepancy between the predicted and the measured indenter displacements at the onset of failure increases as R_f increases, i.e. as the tip geometry tends towards blunt. This trend is summarised in Fig. 8 showing the indenter displacement at the onset of failure δ_f and the total energy absorption E_A for different frontal nose radii. Similar to Fig. 6c, the choice of K has a small overall influence on the total energy absorption predicted by the model (Fig. 8b).

3.3. Discussion

For two families of indenter nose shapes, a variable corner radius and a variable frontal nose radius, the theoretical model is capable of predicting the slope of indenter force-displacement curve reasonably well. In all cases, the slope is consistently higher than the experimental measurements. Note that if K is treated as a modelling parameter, the choice $K = 0.82$ gives excellent agreement with experiments across all nose shapes.

As shown subsequently, using finite element analysis, the omission of friction and boundary compliance in theoretical model may contribute to the discrepancy between the model prediction and experimental results. However, it is believed that the main reason for the remaining discrepancy between model and experiment is the assumption of plane strain ($\varepsilon_{\theta\theta} = 0$). As shown by the numerical simulations of Lee et al. (2004), this assumption is valid only when a rough contact exists between the indenter and plate (i.e. coefficient of friction $\mu = 1$). For a frictionless contact (i.e. $\mu = 0$), biaxial stress is a more valid assumption which results in $\varepsilon_{rr} = \varepsilon_{\theta\theta} = -2\varepsilon_{zz}$. Determining σ_{rr} and t in Equation (17) for this condition however, needs an explicit geometrical description of the in-plane displacement. For contacts with the non-zero coefficient of friction, the stress state becomes very complex and the indentation response cannot be predicted with a simple theoretical

model.

To predict the total energy absorbed accurately, the displacement at failure also needs to be precisely captured. Although the model is successful in predicting the onset of failure for R_f/R_f (for the variable tip radius case) and for R_{ch}/R_f (for the variable chamfer radii) ranging between 0.5 and 1, the discrepancy with the experiment grows in both cases as the indenter tends to blunt (or flat), i.e. as R_f/R_f and R_{ch}/R_f approached zero. This can be explained again by the modelling assumptions given in Equation (5). As the nose shape approaches the blunt limit, the contribution of shear stress locally at the indenter perimeter cannot be ignored, even for thin plates. The assumption of plane stress also breaks down if deformation localises at the indenter perimeter. In the next section, the problem will be re-assessed using finite element analysis. The effect of including more refined constitutive models, for both plasticity and the onset of damage, and the more precise modelling of other physical conditions (such as boundary compliance) will be discussed.

4. Numerical investigation

The finite element model development is first outlined. The model is then applied to predict the quasi-static punch indentation response of the 1 mm thick aluminium alloy plates, for both indenter nose shape types (variable chamfer radius, and variable tip radius). Comparisons are made with the experimental results, and the accuracy of the numerical predictions assessed, across the wide range of deformation states generated by this range of tip geometries.

4.1. Elastic-plastic constitutive response

The elastic response of aluminium alloy 6082-T4 plate is modelled using isotropic linear elasticity, with Young's modulus $E = 70$ GPa and Poisson's ratio $\nu = 0.33$. For the plastic deformation, the Hill (1948) anisotropic model is used. The anisotropy constants, defined in Equations (3–4), are listed in Table 1. The strain hardening of the material is obtained using the true stress-strain curve obtained from the engineering values given in Fig. 2. In order to extrapolate the hardening response beyond the onset of necking in the tensile tests, a power law function, Equation (7), is fitted to the true stress-strain data. The fitting constants obtained for the aluminium alloy sheet are given in Table 1. Because the in-plane anisotropy is small, this fit (obtained for the dog-bone machined parallel to the rolling direction) is assumed for all in-plane directions. To ensure a smooth transition between the measured strain hardening data and the power law fit, the measured hardening curve is used up to a true tensile strain of 0.1 (where the experimental data and power law fit coincide). For larger strains, the power law relationship is then assumed.

4.2. Damage model

Accurate prediction of the onset of ductile damage and failure in the metal plate is a key element of the numerical modelling. In order to predict the onset of damage over a wide range of different stress states, the modified Mohr-Coulomb (MMC) model proposed by Bai and Wierzbicki (2009) is used. This model predicts a critical equivalent plastic strain at the onset of failure, in terms of both the stress triaxiality and the Lode angle. In the MMC model, the onset of failure is taken to occur when the damage indicator:

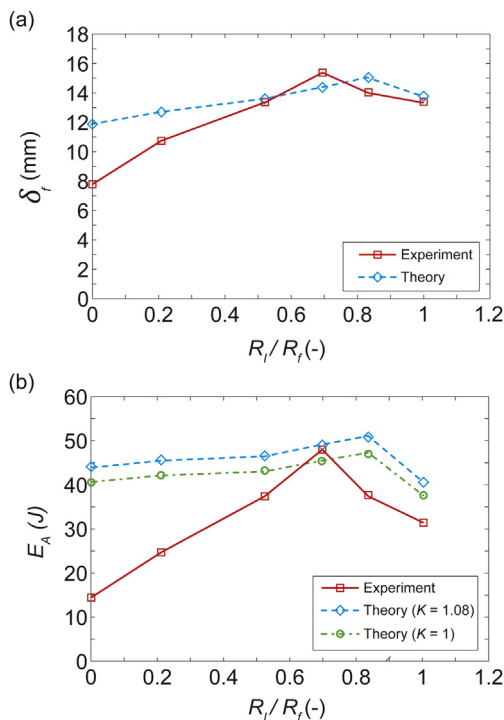


Fig. 8. Comparison of the experimental results and the theoretical model predictions for (a) the displacement at failure δ_f and (b) the absorbed energy E_A for $0 \leq R_f/R_f \leq 1$. (b) also shows the effect of the modelling constant K on the predicted energy absorption.

$$D = \int_0^{\bar{\epsilon}_p} \frac{d\bar{\epsilon}_p}{f(\eta, \bar{\theta})} = 1. \quad (27)$$

Here, $\bar{\epsilon}_p$ is the equivalent plastic strain. The stress triaxiality:

$$\eta = \frac{\sigma_m}{\bar{\sigma}}, \quad (28)$$

where σ_m is the mean stress and $\bar{\sigma}$ is the equivalent stress. The Lode parameter $\bar{\theta}$ is defined by:

$$\bar{\theta} = 1 - \frac{6\theta}{\pi} = 1 - \frac{2}{\pi} \arccos(\xi), \quad (29)$$

where θ is the Lode angle and:

$$\xi = \left(\frac{J_3}{\bar{\sigma}} \right)^3 \quad (30)$$

where J_3 is the third invariant of the deviatoric stress tensor. In the case that η and $\bar{\theta}$ are constant throughout the deformation, Equation (27) can be integrated and the equivalent plastic strain at the point of fracture ($D = 1$) is given by:

$$\bar{\epsilon}_f = f(\eta, \bar{\theta}). \quad (31)$$

By excluding the dependency on pressure and Lode angle from the generalised hardening rule proposed by Bai and Wierzbicki (2008), the MMC model reduces to:

$$\bar{\epsilon}_f = \left\{ \frac{A}{c_2} \left[\sqrt{\frac{1+c_1^2}{3}} \cos\left(\frac{\bar{\theta}\pi}{6}\right) + c_1 \left(\eta + \frac{1}{3} \sin\left(\frac{\bar{\theta}\pi}{6}\right) \right) \right] \right\}^{-\frac{1}{n}}. \quad (32)$$

Thus, in addition to the hardening parameters A and n (given in Table 1), the two parameters c_1 and c_2 also need to be calibrated. Since in many cases η and $\bar{\theta}$ are not constant during the deformation, an average up to the point of fracture:

$$\eta_{avg} = \frac{1}{\bar{\epsilon}_f} \int_0^{\bar{\epsilon}_f} \eta(\bar{\epsilon}_p) d\bar{\epsilon}_p \quad (33)$$

$$\bar{\theta}_{avg} = \frac{1}{\bar{\epsilon}_f} \int_0^{\bar{\epsilon}_f} \bar{\theta}(\bar{\epsilon}_p) d\bar{\epsilon}_p,$$

is normally used for calibration purposes (Bai and Wierzbicki, 2009; Wierzbicki et al., 2005). The process used to obtain the constants for the aluminium alloy 6082-T4 used in the current experiments is described in the following section.

4.2.1. Outline of the calibration procedure

In order to calibrate the parameters in Equation (32), at least two values for the equivalent plastic strain at failure ($\bar{\epsilon}_f$) at different values of η and $\bar{\theta}$ are needed. Measuring the failure strain, especially for specimens in sheet form, is challenging. Because of inhomogeneous deformation inside the neck, and variations in strain across the gauge section prior to failure initiation, local measurement of strain is needed to obtain the failure conditions accurately. Techniques such as digital image correlation (DIC) are often used to measure the strain at the surface of the specimen. However, the critical strain at the onset of failure can occur at some point through

the thickness of sample, and thus under conditions that are different from those obtained at the surface by DIC (Gruben et al., 2011). In this investigation, a combination of experiment and finite element analysis is used to obtain the fracture strain, as well as average values of η and $\bar{\theta}$ at the critical material point.

4.2.2. Failure characterisation experiments

Two material characterisation experiments are performed to obtain the equivalent plastic strain at failure under two different states of stress. Firstly, the results of the tensile tests presented in Section 2 are used. Secondly, tensile tests on notched specimens are conducted. The geometry of the notched specimen is identical to that of Beese et al. (2010) and is illustrated in Fig. 9a. In all cases, 1 mm thickness aluminium alloy 6082-T4 sheet material is used. Due to the low in-plane anisotropy of the sheet, in what follows all specimens are tested only parallel to the rolling direction.

The quasi-static tensile response of the notched specimen is shown in Fig. 9b. Three repeat tests (not shown here) were performed which indicated a good repeatability. The tensile tests were conducted at a test machine cross head speed of 0.72 mm min^{-1} . This speed is chosen to produce approximately the same nominal strain rate as for tensile tests on the dog-bone specimens. However, it should be noted that deformation is not uniform across gauge section of the notched specimen. Two laser tags were mounted on the specimen, outside the gauge section, at an initial spacing of approximately 26 mm. The data obtained from the laser extensometer is used to provide the displacement measurements in Fig. 9b.

4.2.3. Finite element modelling of characterisation experiments

Finite element analysis of the calibration tests was performed using Abaqus/standard V6.12. Both characterisation experiments were modelled in 3D, with the geometry discretised using linear continuum elements with eight nodes and reduced integration (C3D8R in Abaqus notation (Abaqus, 2010)). The geometry of the tensile dog-bone and notched specimen models were identical to those used in experiments. The region of the test specimens outside of the test machine grips was modelled, as shown in Fig. 10. One end of the specimen was fully clamped, and a displacement boundary condition was applied to the other end, to simulate the motion of the cross-head. The elastic-plastic constitutive model defined in Section 4.1 was used, but no damage or failure was included in these simulations. The purpose of the model is not to predict fracture, but to compute the state of deformation of the material at the point at which failure was seen to occur in the experiments.

4.2.3.1. Mesh sensitivity. Finite element analysis of necking phenomena can be sensitive to the size of the mesh. To assess this effect, three mesh sizes were considered for the gauge section of both test specimen geometries, denoted meshes 1, 2 and 3. For the dog-bone specimens, the smallest element sizes in each case are 0.33 mm, 0.17 mm and 0.11 mm respectively. For the notched specimens, the smallest element sizes at the centre of the specimens are in each case $0.40 \times 0.90 \times 0.25 \text{ mm}$, $0.31 \times 0.22 \times 0.17 \text{ mm}$ and $0.16 \times 0.13 \times 0.08 \text{ mm}$ respectively. This means that 4, 6 and 12 elements are used through the thickness of the specimen, respectively.

The results of the mesh sensitivity investigation are plotted in Fig. 11a for the tensile dog-bone and in Fig. 12a for the notched specimen. It should be noted that the displacement shown for the numerical simulations in Figs. 11 and 12 is the relative displacement between two points in the FE model which are located in the same position as the laser tags in the experiments. Up to the point of necking there is no difference in the results of the three mesh

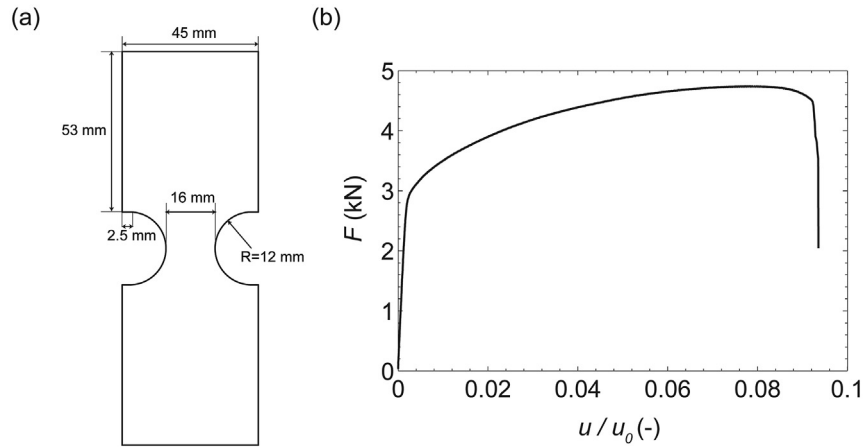


Fig. 9. (a) The geometry of the notched specimen used (similar to (Beese et al., 2010)) for the material characterisation. (b) The quasi-static tensile response of a notched specimen of aluminium alloy 6082-T4 oriented parallel to the rolling direction. u represents the separation of the reference points (defined by the edge of the laser tags) and u_0 represents the initial separation.

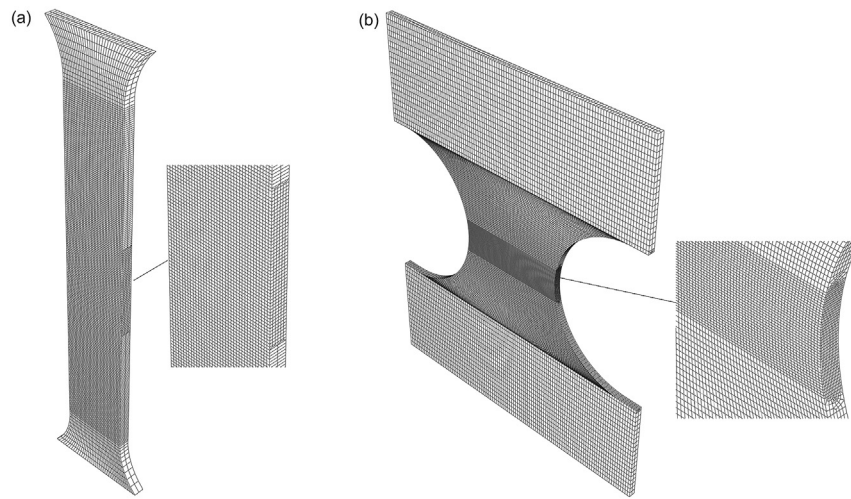


Fig. 10. Finite element models for (a) the dog-bone specimen and (b) the notched specimen.

sizes. As the deformation becomes inhomogeneous, significant mesh sensitivity is observed. A larger drop in force occurs for a finer mesh, which more closely matches the post-necking softening behaviour in the experimental data. Note that comparison with the experiment is only valid up to fracture of the metal, since no damage or fracture is included in these numerical calculations.

4.2.3.2. Anisotropy. In order to assess the sensitivity of the response to material anisotropy, the calculations were repeated with an isotropic plastic response. In what follows, the finer mesh 3 was used. The results are shown in Figs. 11b and 12b. For tensile tests on dog-bone specimens (Fig. 12b), no difference can be seen during the homogenous deformation phase. However, anisotropy significantly affects the post-necking behaviour. For the notched specimen, the difference between isotropic and anisotropic plasticity models is apparent immediately after yield. The anisotropy also seems to affect the onset of necking in this case. In what follows, the anisotropic yield surface will be used.

4.2.3.3. Fitting the MMC model. Next, the two fracture model coefficients (c_1 and c_2) are to be determined, using the equivalent plastic strain at the onset of fracture failure ($\bar{\epsilon}_f$) for the two different

loading conditions (i.e. different values of η_{avg} and $\bar{\theta}_{avg}$). In Figs. 11c and 12c, the evolution of equivalent plastic strain, obtained from the FE calculations, for the critical material point (defined as the point with the maximum equivalent plastic strain) is shown for the dog-bone and notched specimens. The critical material point is located inside the neck and at mid-thickness of the samples in both cases. The location of the critical material point in the notched specimen is found to be at the centre of the plate, away from the edges, confirmed by both the FE simulations and DIC results obtained during the experiment. The solid vertical line in Figs. 11c and 12c shows the displacement (obtained from the laser extensometer) at which failure occurs for the experimental specimens. The crossing point of the numerical simulation results with this vertical line is considered to be the equivalent plastic strain at the onset of the failure. Comparing the values of $\bar{\epsilon}_f$ obtained for the three different mesh sizes, it is seen that mesh 3 is sufficiently fine, and further refinement will not change the value significantly. Figs. 11d and 12d show the history of the stress triaxiality and normalised Lode angle throughout the deformation at the critical point, for mesh 3 and the anisotropic plasticity model. As the values of η and $\bar{\theta}$ are not constant, an average (Equation (33)) is taken up to the point of failure, represented by the solid line in Figs. 11d and 12d. The

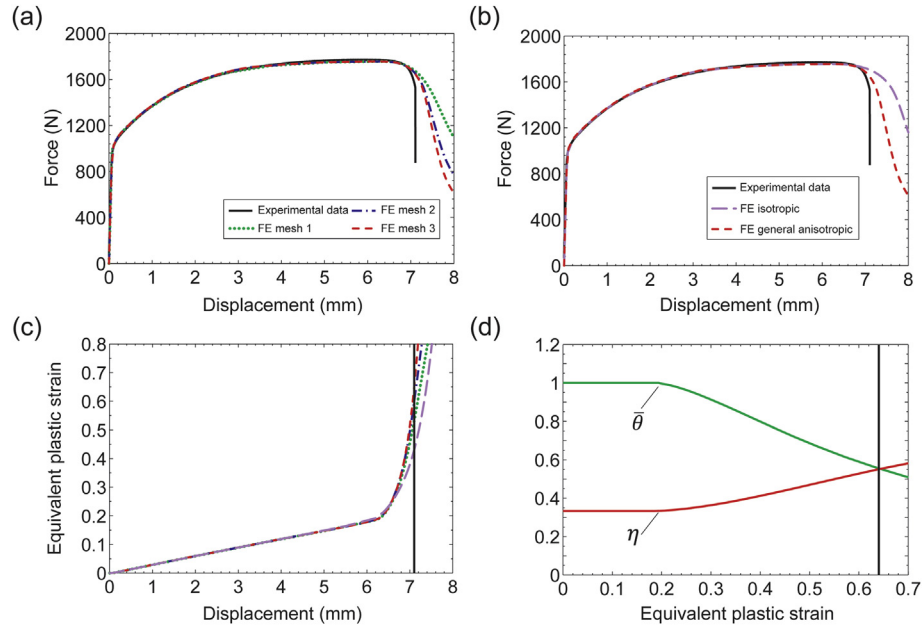


Fig. 11. The effect of (a) finite element mesh size and (b) material anisotropy on the predicted uniaxial tensile response of the dog-bone specimen. (c) and (d) show the evolution of the equivalent plastic strain and the stress state (η and $\bar{\theta}$) in the critical element during deformation.

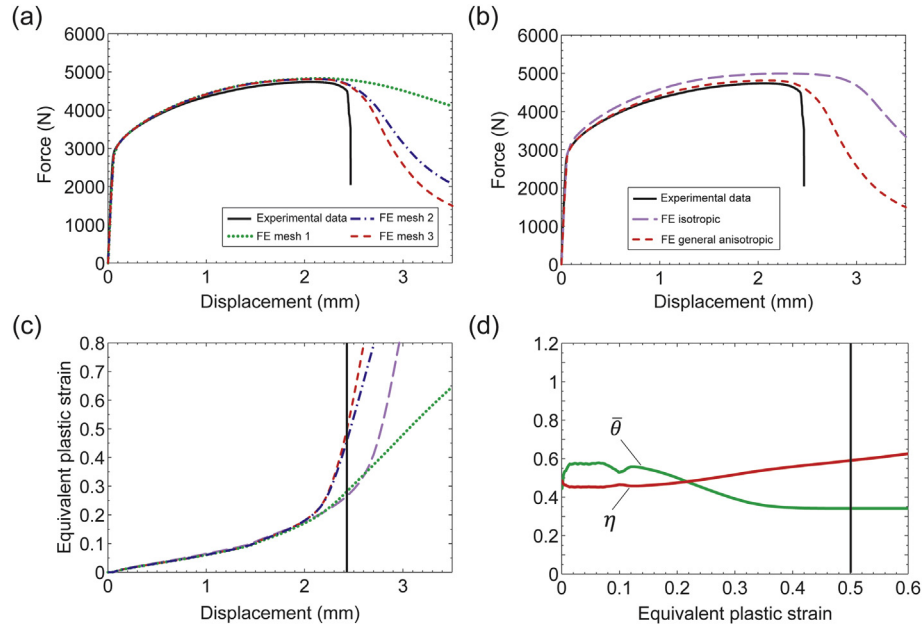


Fig. 12. The effect of (a) finite element mesh sensitivity size and (b) material anisotropy on the predicted uniaxial tensile response of the notched specimen. (c) and (d) show the evolution of the equivalent plastic strain and the stress state (η and $\bar{\theta}$) in the critical element during deformation.

conditions at failure obtained from both test specimens are listed in Table 2.

Finally, the surface defining the failure strain in stress triaxiality-Node parameter space, given by Equation (32), is fitted to these data

points. An optimisation routine is used in order to find the best fit for this surface through the two experimental data points. The coefficients obtained are $c_1 = 0.003$ and $c_2 = 232$ MPa.

4.3. Punch indentation simulations

In this section, the quasi-static indentation experiments described in Section 2.2 are modelled using finite element method. First, a 3D finite element model is developed for indentation of a plate by a hemi-spherical indenter. Parameters influencing the response including boundary condition, anisotropy and friction are

Table 2

Fracture conditions for dog-bone and notched specimens.

Test	$\bar{\epsilon}_f$	η_{avg}	$\bar{\theta}_{avg}$
Tensile (dog-bone)	0.63	0.398	0.856
Tensile (notched)	0.50	0.507	0.451

investigated. Secondly, an axisymmetric FE model is developed and the numerical results are compared with experiment for both types of indenter shape described in Section 2.2.

4.3.1. Numerical model development

4.3.1.1. 3D simulations. A quarter plate model was simulated in 3D using Abaqus/standard V6.12 for loading with a hemi-spherical indenter. To assess the significance of boundary compliance, the clamping conditions used in the experiments (shown in Fig. 1c) were simulated in detail. The FE model is shown in Fig. 13. Symmetry boundary conditions applied along the free edges of the quarter plate model. As well as the circular test area, the region of the plate under the clamping ring and the retaining bolts were included. The retaining bolts were modelled as cylindrical rigid pins, discretised using rigid elements with four nodes (R3D4). Frictionless contact was defined between these retaining pins and the plate. The indenter was also modelled as rigid (discretised using element type R3D4). Note that no deformation of the indenter was observed during the experiments. The plate was modelled using solid elements with eight nodes and reduced integration (C3D8R). The mesh in regions of the plate close the indenter was refined to a typical element size of $0.42 \times 0.42 \times 0.25$ mm. It was found that the simulation results were insensitive to further refinement of the mesh. Coulomb friction was used between the indenter and the plate with a coefficient of friction $\mu = 0.25$ (unless specified otherwise). This is a typical value for the dynamic coefficient of friction for steel sliding on aluminium (Waterhouse, 1992). The anisotropic material model outlined in Section 4.1 with the MMC damage model was used for the plate (unless specified otherwise).

First, the influence of the boundary conditions is investigated. Two cases are considered:

1. Fully clamped boundary. Here, all degrees of freedom in the “clamping area” defined in Fig. 13 are constrained to be zero.
2. Compliant boundary. In this case, only the vertical degrees of freedom at the surface of the plate in the “clamping area” are constrained to be zero. The nodes are free to translate in the horizontal plane, with pull-out constrained by the retaining

pins. This condition represents the presence of a clamping ring with frictionless contact between it and the specimen plate.

Results from these two cases are plotted in Fig. 14a. The simulation results indicate slight yielding around the holes in the clamping area in the compliant boundary case. This allows the material in this area to pull towards the centre of the plate. Although the amount of pull-out is very small (around 0.15 mm) this compliance reduces the slope of the indenter force-displacement response (Fig. 14a). When the compliance is included, the response matches the experiment well (Fig. 14a). This can explain part of the discrepancy observed in Fig. 5 between the theory and the experiment, as the effect of boundary compliance was not considered in the model presented in Section 3.

Next, the effect of material anisotropy is investigated. For these simulations compliant grip conditions are used. The results are shown in Fig. 14b for both anisotropic and isotropic cases. In the latter, the yield strength and strain hardening follow that measured in the rolling direction. Anisotropy has a significant effect on the force-displacement curve. Introducing anisotropy reduces the slope of the force-displacement curve, and again appears to be essential to provide a close match with the experiment. A similar observation was reported by Beese et al. (2010).

Finally, the effect of the friction coefficient between the indenter and the plate is shown in Fig. 14c. The response is less sensitive to friction than to either compliance or anisotropy, with the friction coefficient only influencing the later stages of deformation. Comparison with the experiment confirms the choice of $\mu = 0.25$, which gives the closest match. It should be noted however, as discussed in Section 3.4, the choice of friction coefficient has a strong influence on the stress state of the material and the validity of the assumptions made in the theoretical model presented in Section 3.

In summary, it can be concluded from the 3D model that correct agreement between simulation and experiment requires that the boundary compliance, anisotropy and indenter-plate friction coefficient are all accounted for accurately.

4.3.1.2. Axisymmetric model development. The 3D finite element

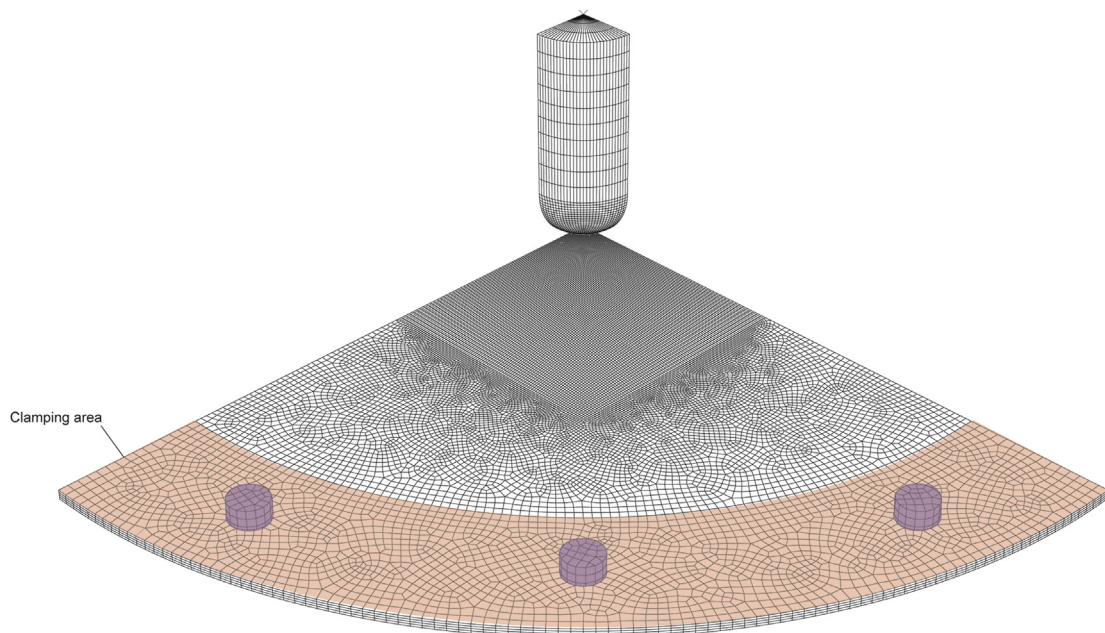


Fig. 13. 3D finite element model of the punch indentation with a hemi-spherical indenter.

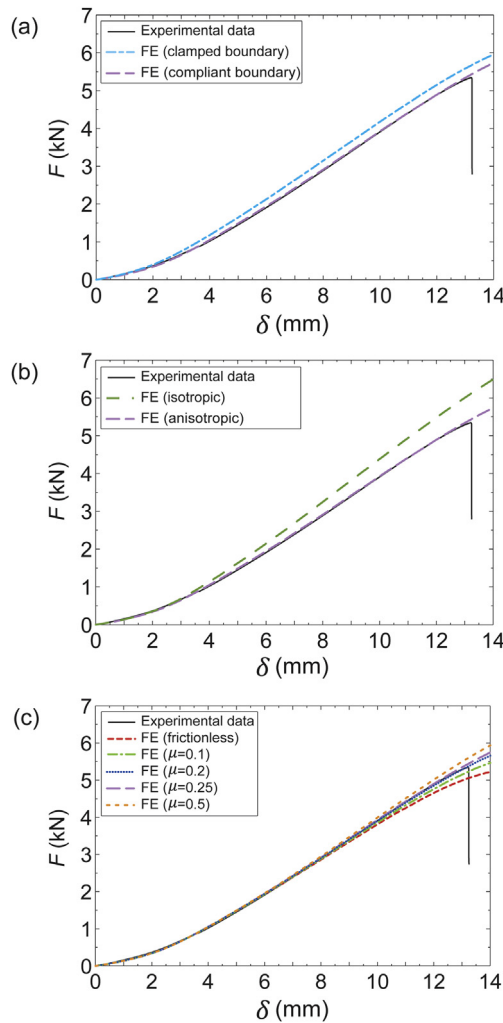


Fig. 14. The effect of (a) grip compliance, (b) material anisotropy and (c) the indenter-plate friction coefficient on the indentation response of 1 mm thickness aluminium alloy 6082-T4 by a hemi-spherical indenter. δ is the indenter displacement and F is the indenter force.

models of the plate indentation are numerically expensive. This limits the mesh refinement possible, which becomes a limitation for indenters with higher local curvatures. An axisymmetric calculation is therefore desirable. Since the material investigated here, aluminium alloy 6082-T4, shows only transverse anisotropy (Table 1), the simplification of the FE model to 2D is appropriate. This however, might not be true for all metallic alloys. For materials with general anisotropy, the 3D model presented in the previous section should be used instead. The development of this 2D model is described next.

The axisymmetric model (Fig. 15a) was developed using Abaqus/explicit V6.12. The explicit time integration version of Abaqus was used for these quasi-static calculations, as the explicit solver is more efficient for problems involving contact. Axisymmetric continuum elements with four nodes and reduced integration (CAX4R) were used to discretise the aluminium plate and the indenter was modelled using axisymmetric rigid elements with two nodes (RAX2). The majority of the plate was meshed with four elements through the thickness with element size of 0.25×0.25 mm. Local mesh refinement under the indenter chamfer was necessary. This was optimised separately for each indenter geometry. The mesh size in this zone was 0.03×0.03 mm for smaller chamfer radii

($R_{ch} = 0.1$ and 1.5 mm) and 0.12×0.12 mm for larger chamfer radii ($R_{ch} \geq 3$ mm). In each case, mesh insensitivity was verified. In this two-dimensional model, in-plane anisotropy is neglected. As shown in Fig. 2 and Table 1, the in-plane anisotropy is very small compared to the transverse anisotropy. Separate 3D calculations were performed to confirm that this simplification has a negligible effect on the calculated indentation response. For this reason, only the anisotropy constant R_{33} is included and all of the other coefficients in Table 1 are considered to be equal to 1. In these simulations, failure of the plate is not modelled directly. However, the MMC damage criterion defined previously is implemented, and the calculation stopped when failure initiation ($D = 1$) is first calculated at any location in the model. The MMC failure locus, defined by Equation (32), is implemented in Abaqus in tabular form.

In order to model the grip compliance in the axisymmetric model, a non-linear spring is introduced at the edge of the plate, as shown in Fig. 15a. A similar approach has been used by Grytten et al. (2007). The spring is one-dimensional and only allows translation of the edge of the plate in the horizontal direction. In contrast to (Grytten et al., 2007), who adopted a linear spring, the response of the spring is considered to be bi-linear (Fig. 15b) and calibrated such that the prediction of the axisymmetric FE model gives the closest match to the indentation experiment for the hemi-spherical indenter case. The response of the spring is then kept fixed for all of the other indenter geometries. A bi-linear stiffness is necessary to represent the extra compliance that occurs due to yielding of the plate material around the retaining pins. The indenter geometries used in the 2D calculations match those described previously for the experimental investigation. In the case of the flat nosed (i.e. blunt) indenter, a small chamfer radius of 0.1 mm, which is one tenth of plate thickness, was introduced to remove the stress singularity at a perfectly sharp edge (Fig. 15a). In each calculation, the indenter was displaced 20 mm in 0.1 s using the Abaqus “smooth step” amplitude function, to minimise oscillations in the response. This (artificially high) indentation rate, in addition to mass scaling, was selected to reduce computational time. A fixed mass scaling of 100 was applied to the whole model, which means increasing the overall mass (or density) of the model by a factor of 100 . Since the square time increment for the explicit solver is proportional to the square root of density, the mass scaling decreases the computational time by a factor of 10 . Kinetic energy was less than 5% of the internal energy in all cases, which confirms that dynamic effects are negligible.

4.3.2. Modelling results and discussion

A comparison between experimental and numerical results is shown in Fig. 16a and b for indenters with different chamfer radii and frontal nose radii respectively. The cross indicates the point at which the first onset of failure ($D = 1$) was calculated in the numerical models. A good agreement between experiment and model prediction can be seen for both series of indenter shapes. In all cases, the predicted slopes of the force-displacement curves closely match the experiments. The point of failure in the plate is also successfully captured by the finite element simulations with the exception of indenters with sharper edges (e.g. flat and $R_f = 30$ mm).

4.3.2.1. Variable chamfer radii. Consider first the simulation results for indenters with different chamfer radii. In Fig. 17, a comparison is made between experiments and finite element calculations of the indenter displacement at failure (δ_f) and the total absorbed energy up to first failure (E_A), defined as the area under the indenter force-displacement curve. It can be seen that the MMC failure model leads to an accurate prediction of these performance criteria. To assess the importance of the failure model, the calculations were

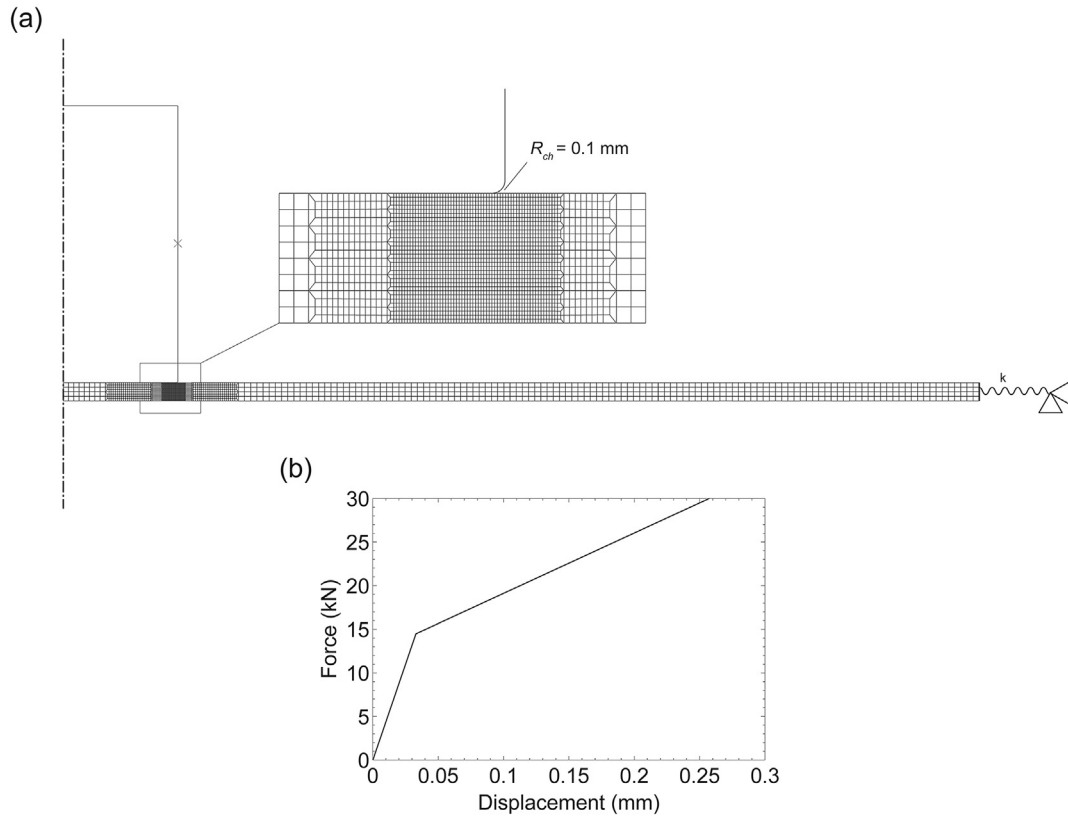


Fig. 15. (a) Axisymmetric finite element model of a 1 mm thick aluminium alloy plate loaded by a flat (blunt) indenter. (b) The response of the bi-linear spring used for modelling the compliance at the grip in the axisymmetric FE model.

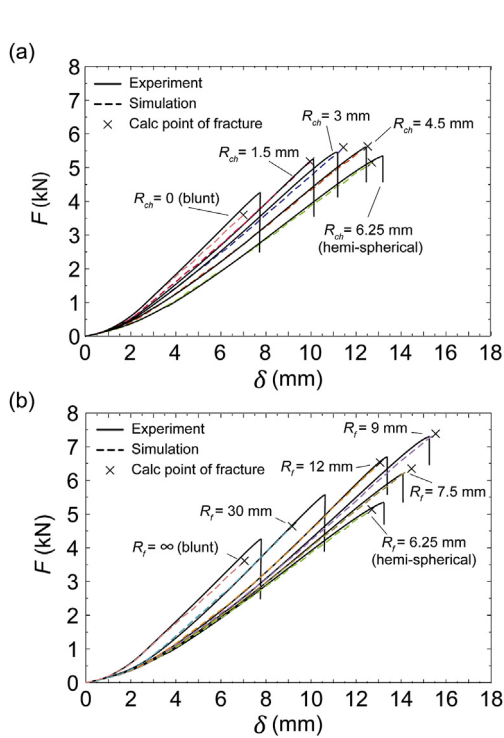


Fig. 16. A comparison between experimental results and finite element model predictions (using the MMC damage model) for indenters with (a) different chamfer radii and (b) different frontal nose radii.

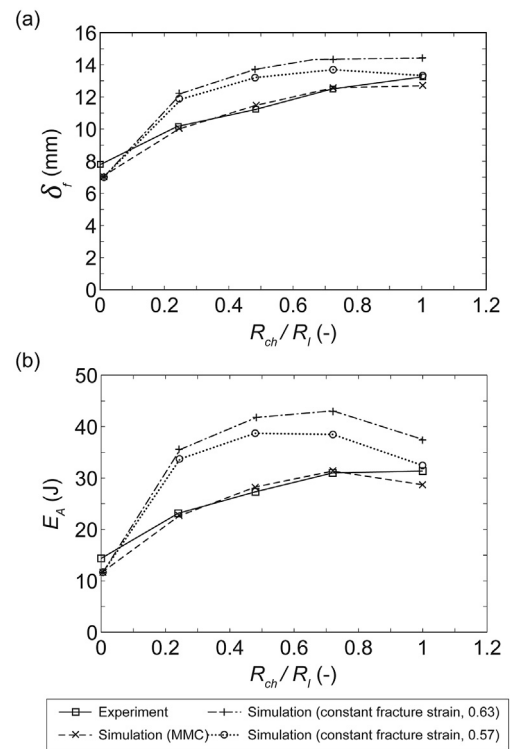


Fig. 17. A comparison between experimental results and finite element model predictions (using both a constant failure strain criterion and the MMC damage model) for punch indentation using different chamfer radii (R_{ch}). (a) The indenter displacement at failure δ_f and (b) the energy absorption up to failure (E_A).

repeated with simpler, constant failure strain criteria (i.e. $\bar{\epsilon}_f$ specified to be independent of stress state). First, a constant fracture strain criterion with $\bar{\epsilon}_f = 0.63$ (the value obtained from the dog-bone tensile experiments) is considered. As can be seen in Fig. 17, the comparison indicates a poor agreement with experiment. Next, a constant fracture strain criterion with $\bar{\epsilon}_f = 0.57$ is considered. This value was chosen iteratively, so that the calculation matched the indentation experiment with a hemi-spherical indenter (which might be considered an alternative strategy for determining the failure criterion). Again, there is still poor agreement between simulation and experimental results when a range of different chamfer radii are considered, with the biggest deviation occurring for a chamfer radius of 3 mm. These results confirm that a simple failure strain criterion is incapable of predicting failure for different indenter chamfer radii. Although the MMC fracture model slightly under predicts the energy absorption for hemi-spherical and flat indenters, a much closer overall match with experiment is observed.

Fig. 18 gives the calculated stress triaxiality and normalised Lode angle versus equivalent plastic strain at the critical material point up to the point of failure initiation. As can be inferred from Fig. 18a, for all chamfer radii except $R_{ch} = 0.1$ mm (the flat indenter), the stress triaxiality remains constant throughout the deformation ($\eta \approx 2/3$). The fracture initiates from the distal surface in these cases. In contrast, for a flat indenter, the critical material point is located under the indenter edge on the contacted face and experiences large, negative values of η (Fig. 18a) as a result of the high contact pressure. Although the values of stress triaxiality for $R_{ch} \geq 1.5$ mm are similar, they have different values of the normalised Lode angle ($\bar{\theta}$). For a hemi-spherical indenter, $\bar{\theta}$ approaches -1 at failure, indicating an equi-biaxial stress state ($\eta = 2/3$). By decreasing the chamfer radius the average value of $\bar{\theta}$ is reduced. For small chamfer radii (0.1 and 1.5 mm) $\bar{\theta}$ is closer to zero which

indicates plane strain conditions at the critical point (Fig. 18b).

These results indicate the importance of accounting for the Lode angle, which emerges as the most discriminating parameter for the critical material point for the different indenter nose shapes. If a failure model were to only include a dependency on the stress triaxiality (e.g. the Johnson-Cook damage model), the plate would fail at almost the same plastic strain for all of the indenters with $R_{ch} \geq 1.5$ mm, which would not reproduce the experimental results well. The difference in the failure strain for each nose shape, at least for $R_{ch} \geq 1.5$ mm, seems to originate primarily from the variation in $\bar{\theta}$.

4.3.2.2. Variable tip radius. Consider next, the simulation results using indenters with different frontal nose radii. The comparison with experiment is shown in Fig. 19a. A good agreement can be seen across the full range of nose shapes. A peak in energy absorption is seen at $R_f = 9$ mm, which corresponds to a transition in the mode of failure, as revealed clearly by the FE calculations. This transition in the failure mode is in agreement with the observation of Corran et al. (1983), who also reported a maximum in energy absorption for a 1.3 mm thick steel plate.

An example of the calculated damage distribution just before failure initiation, and a picture of the corresponding failed plate from the experiments, is shown in Fig. 19b. For $R_f < 9$ mm (e.g. $R_f = 7.5$ mm) the damage predicted by the FE model is more widely distributed below the indenter and fracture initiates from the distal surface. Tensile failure occurs in these cases. For $R_f > 9$ mm however, close to the point of failure, the damage becomes localised in a narrow band under the edge of the indenter, where failure occurs. An example of this can be seen in Fig. 19b for $R_f = 12$ mm. In this case the maximum damage occurs at the distal surface. For $R_f > 12$ mm failure initiates instead at the proximal surface, below the edge of the indenter. This failure mechanism can be considered shear-dominated plugging.

According to Fig. 19a, the largest discrepancy between experimental and finite element results can be found for these radii ($R_f > 12$ mm). This can be attributed to premature failure in the numerical simulations, due to inaccuracies in the calibrated failure strain locus in stress space (Equation (32)) for shear dominated stress states, which lie away from the two experimental points used to fit the surface. These points were well separated in the $\bar{\theta}$ direction, but are close in stress triaxiality. For the model to perform better under negative stress triaxialities, additional calibration data points with low stress triaxialities are needed (e.g. compression and shear tests).

5. Conclusions

In this paper, the effect of the indenter nose shape on the deformation and failure of thin, monolithic metal plates (1 mm thick aluminium alloy 6082-T4) is investigated. The shape of the indenters is gradually changed from flat to hemi-spherical either by increasing the chamfer radius or by increasing the frontal nose radius, thus producing a wide range of stress-states at the onset of failure. This poses a challenge to the predictive accuracy of modelling techniques, and through the application of both analytical and finite element models, we interrogate the importance of key modelling parameters. This understanding is particularly important for indentation scenarios where the effective indenter tip geometry is unknown, for example when polymer coatings are used to enhance perforation resistance (Mohagheghian et al., 2016). The following conclusions are drawn:

- The theoretical model proposed by Simonsen and Lauridsen (2000) for hemi-spherical indenters, is extended to account

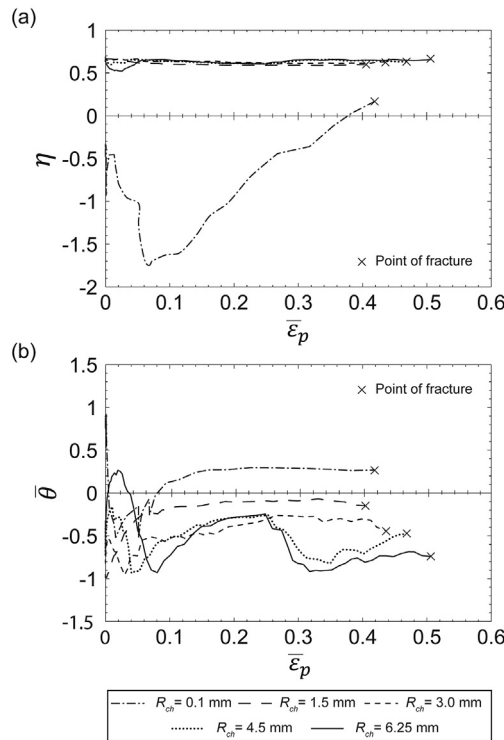


Fig. 18. Variation in (a) the stress triaxiality η and (b) the normalised Lode angle $\bar{\theta}$ for the critical material point up to the onset of failure initiation, for indenters with different chamfer radii (R_{ch}).

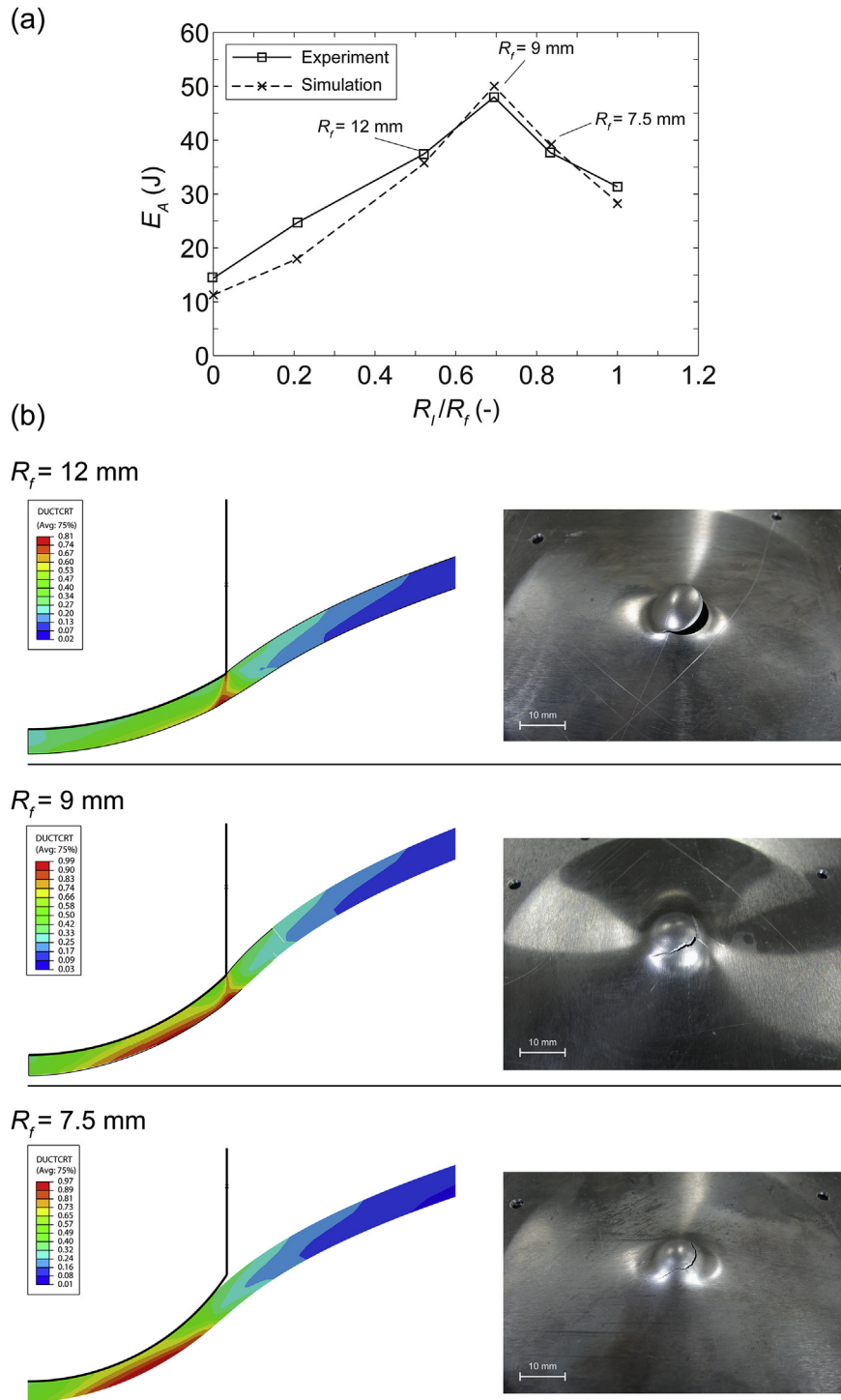


Fig. 19. (a) A comparison between experimental results and finite element model predictions (using the MMC damage model) of the energy absorption up to fracture (E_A) for punch indentation using different frontal nose radii (R_f). (b) The predicted damage distribution (left column) and pictures of failed plates (right column) for indenters with frontal nose radii of $R_f = 7.5$ mm, $R_f = 9$ mm and $R_f = 12$ mm.

for the complete range of tip geometries considered here. The model successfully captures the change in the indentation response with variations in the indenter nose shape. However, in all cases, the indenter force predicted by the model is consistently 20% higher than that of the experiment. This is believed to be the result of the kinematic assumption of zero transverse strain. The accuracy of the model prediction

improves further when anisotropy of the material is considered. If K is treated as a modelling parameter, the choice $K = 0.82$ gives excellent agreement with experiments across all nose shapes.

- The theoretical model predicts the indenter displacement at failure (δ_f) accurately for the range of nose shapes R_{ch}/R_i and $R_i/R_f > 0.5$. As both indenter variations approach a flat (i.e. blunt) tip geometry, a larger discrepancy is observed. This is due to a

violation of the modelling assumption that the deformation is dominated by membrane tensile stretching, as the deformation in fact localises under the edge of the indenter in these cases.

- In order to predict the indentation response using finite element analysis, an anisotropic yield surface (in this case the (Hill, 1948) model) and a damage model accounting for both the stress triaxiality and the Lode angle is necessary. The Lode angle dependency is essential for predicting the indentation response across a wide range of tip geometries.
- The finite element analysis must also account for (i) indenter-plate friction and (ii) boundary compliance to provide an accurate prediction of the experimental response.

Acknowledgment

The authors are grateful for joint financial support from the Engineering and Physical Sciences Research Council (EPSRC) and the Defence Science and Technology Laboratory (DSTL) through project EP/G042756/1 (Polymer Nanocomposites for Light Armour Applications).

References

- Abaqus, 2010. Abaqus v6.12 Documentation- ABAQUS Analysis User's Manual.
- ASTM E8/E8m-11, 2011. Standard Test Methods for Tension Testing of Metallic Materials. <http://dx.doi.org/10.1520/E0008>.
- Bai, Y., Wierzbicki, T., 2009. Application of extended Mohr–Coulomb criterion to ductile fracture. *Int. J. Fract.* 161, 1–20. <http://dx.doi.org/10.1007/s10704-009-9422-8>.
- Bai, Y., Wierzbicki, T., 2008. A new model of metal plasticity and fracture with pressure and Lode dependence. *Int. J. Plast.* 24, 1071–1096. <http://dx.doi.org/10.1016/j.iplas.2007.09.004>.
- Beese, A.M., Luo, M., Li, Y., Bai, Y., Wierzbicki, T., 2010. Partially coupled anisotropic fracture model for aluminum sheets. *Eng. Fract. Mech.* 77, 1128–1152. <http://dx.doi.org/10.1016/j.engfracmech.2010.02.024>.
- Colby, R.B., 2013. Equivalent Plastic Strain for the Hill's Yield Criterion under General Three-dimensional. Massachusetts Institute of Technology.
- Corran, R.S.J., Shadbolt, P.J., Ruiz, C., 1983. Impact loading of plates — an experimental investigation. *Int. J. Impact Eng.* 1, 3–22. [http://dx.doi.org/10.1016/0734-743X\(83\)90010-6](http://dx.doi.org/10.1016/0734-743X(83)90010-6).
- Eberl, C., Thompson, R., Gianola, D., Sharpe, W.J., Hemker, K., 2006. Digital Image Correlation and Tracking. Mathworks File Exch. <http://www.mathworks.com/matlabcentral/fileexchange/12413>.
- Gruben, G., Fagerholt, E., Hopperstad, O.S., Børvik, T., 2011. Fracture characteristics of a cold-rolled dual-phase steel. *Eur. J. Mech. A/Solids* 30, 204–218. <http://dx.doi.org/10.1016/j.euromechsol.2011.01.004>.
- Grytten, F., Børvik, T., Hopperstad, O.S., Langseth, M., 2009. Quasi-static perforation of thin aluminium plates. *Int. J. Impact Eng.* 36, 486–497. <http://dx.doi.org/10.1016/j.ijimpeng.2008.01.015>.
- Grytten, F., Fagerholt, E., Auestad, T., Førre, B., Børvik, T., 2007. Out-of-plane deformation measurements of an aluminium plate during quasi-static perforation using structured light and close-range photogrammetry. *Int. J. Solids Struct.* 44, 5752–5773. <http://dx.doi.org/10.1016/j.ijsolstr.2007.01.026>.
- Gupta, N.K., Iqbal, M.A., Sekhon, G.S., 2007. Effect of projectile nose shape, impact velocity and target thickness on deformation behavior of aluminum plates. *Int. J. Solids Struct.* 44, 3411–3439. <http://dx.doi.org/10.1016/j.ijsolstr.2006.09.034>.
- Hill, R., 1948. A theory of the yielding and plastic flow of anisotropic metals. *Proc. R. Soc. A Math. Phys. Eng. Sci.* 193, 281–297. <http://dx.doi.org/10.1098/rspa.1948.0045>.
- Iqbal, M.A., Gupta, G., Diwakar, A., Gupta, N.K., 2010. Effect of projectile nose shape on the ballistic resistance of ductile targets. *Eur. J. Mech. A/Solids* 29, 683–694. <http://dx.doi.org/10.1016/j.euromechsol.2010.02.002>.
- Kpenyigba, K.M., Jankowiak, T., Rusinek, A., Pesci, R., 2013. Influence of projectile shape on dynamic behavior of steel sheet subjected to impact and perforation. *Thin-Walled Struct.* 65, 93–104. <http://dx.doi.org/10.1016/j.tws.2013.01.003>.
- Landkof, B., Goldsmith, W., 1985. Petalling of thin, metallic plates during penetration by cylindro-conical projectiles. *Int. J. Solids Struct.* 21, 245–266. [http://dx.doi.org/10.1016/0020-7683\(85\)90021-6](http://dx.doi.org/10.1016/0020-7683(85)90021-6).
- Langseth, M., Larsen, P.K., 1994. Dropped objects' plugging capacity of aluminium alloy plates. *Int. J. Impact Eng.* 15, 225–241. [http://dx.doi.org/10.1016/S0734-743X\(95\)80015-6](http://dx.doi.org/10.1016/S0734-743X(95)80015-6).
- Lankford, W.T., Snyder, S.C., Bauscher, J.A., 1950. New criteria for predicting the press performance of deep drawing sheets. *Trans. Am. Soc. Met.* 42, 1197–1232.
- Lee, Y.-W., Woertz, J.C., Wierzbicki, T., 2004. Fracture prediction of thin plates under hemi-spherical punch with calibration and experimental verification. *Int. J. Mech. Sci.* 46, 751–781. <http://dx.doi.org/10.1016/j.ijmecsci.2004.05.004>.
- Leppin, S., Woodward, R.L., 1986. Perforation mechanisms in thin titanium alloy targets. *Int. J. Impact Eng.* 4, 107–115. [http://dx.doi.org/10.1016/0734-743X\(86\)90011-4](http://dx.doi.org/10.1016/0734-743X(86)90011-4).
- Liu, D., Stronge, W.J., 2000. Ballistic limit of metal plates struck by blunt deformable missiles: experiments. *Int. J. Solids Struct.* 37, 1403–1423. [http://dx.doi.org/10.1016/S0020-7683\(98\)00322-9](http://dx.doi.org/10.1016/S0020-7683(98)00322-9).
- Mohagheghian, I., McShane, G.J., Stronge, W.J., 2016. Impact perforation of polymer-metal laminates: projectile nose shape sensitivity. *Int. J. Solids Struct.* 88–89, 337–353. <http://dx.doi.org/10.1016/j.ijsolstr.2016.01.010>.
- Simonsen, B.C., Lauridsen, L.P., 2000. Energy absorption and ductile failure in metal sheets under lateral indentation by a sphere. *Int. J. Impact Eng.* 24, 1017–1039. [http://dx.doi.org/10.1016/S0734-743X\(00\)00024-5](http://dx.doi.org/10.1016/S0734-743X(00)00024-5).
- Teng, X., Wierzbicki, T., 2005. Numerical study on crack propagation in high velocity perforation. *Comput. Struct.* 83, 989–1004. <http://dx.doi.org/10.1016/j.compstruc.2004.12.001>.
- Waterhouse, R.B., 1992. In: Blau, P.J. (Ed.), *ASM Handbook, Friction, Lubrication and Wear Technology*, vol. 18.
- Wierzbicki, T., Bao, Y., Lee, Y.-W., Bai, Y., 2005. Calibration and evaluation of seven fracture models. *Int. J. Mech. Sci.* 47, 719–743. <http://dx.doi.org/10.1016/j.jimecsci.2005.03.003>.